16th World Congress in Computational Mechanics (WCCM)
21-26 July 2024, Vancouver, Canada
A. Korobenko, M. Laforest, S. Prudhomme, R. Vaziri (Eds)

A SELF-STABILIZED TRIANGULAR VIRTUAL ELEMENT FOR KIRCHHOFF–LOVE SHELLS

TIAGO P. WU[1], PAULO M. PIMENTA[1] AND PETER WRIGGERS[2]

[1] Department of Structural and Geotechnical Engineering, University of São Paulo
Av. Prof. Almeida Prado, 83, São Paulo, 05508-070, São Paulo Brazil
tiagowu@usp.br; ppimenta@usp.br

[2] Institute for Continuum Mechanics, Leibniz Universität Hannover
An der Universität 1, Hannover, 30823, Lower Saxony, Germany
wriggers@ikm.uni-hannover.de

Key words: Kirchhoff–Love shells, Linearity, Stabilization-free, Virtual element method.

Abstract. This work presents a self-stabilized triangular virtual element for linear Kirchhoff–Love shells. The domain decomposition by flat triangles directly approximates the shell geometry without resorting to a curvilinear coordinate system or an initial mapping approach. The problem is discretized by the lowest-order conventional virtual element method for the membrane, in which stabilization is needless, and by a stabilization-free virtual element procedure for the plate. Numerical examples of static problems show the potential of the formulation as a prelude for the evolution of self-stabilized Kirchhoff–Love shell virtual elements.

1 INTRODUCTION

Introduced by [1], the virtual element method (VEM) provides arbitrarily polytopal discretizations within the Bubnov–Galerkin framework generalizes the finite element method. Beyond the flexibility to complex computational domain discretizations, the method simplicity relative to higher-order continuity enforcement and additional degrees of freedom is evident, e.g. for the plate problem. On the other hand, in general, a stabilization term must be considered to ensure the method stability or that the stiffness matrix has full rank. Its not unique construction justifies the stabilization-free VEM (SFVEM) development found, e.g. in [2, 3, 4, 5] for the 2D Poisson equation, linear plane elasticity and finite strain applications.

We propose a SFVEM for the present lowest-order conforming plate discretization as an outset for its future evolution. The mathematical model is presented in Section 2 followed by its conventional virtual element discretization in Section 3, found in [6]. The SFVEM is within the latter Section and numerical examples are presented in Section 4.

Unless explicitly indicated, the notations and conventions are Latin and Greek, being regular italic and fraktur lower case letters for scalars (e.g. p, π and $\mathfrak{p}$) and bold for vectors (e.g. $\boldsymbol{p}$, $\boldsymbol{\pi}$ and $\boldsymbol{\mathfrak{p}}$). Bold upright upper case letters are for higher-order tensors (e.g. $\mathbf{P}$ and $\mathbf{\Pi}$) and regular

calligraphic or double-struck for sets (e.g. $\mathcal{P}$ and $\mathbb{P}$). In particular, the null vector is $\mathbf{0}$. Except for τ and ν, regular italic Latin and Greek lowercase indices range over the sets $\{1,2,3\}$ and $\{1,2\}$, respectively (Einstein summation). Depending on the context, subscripts α and 3 respectively mean membrane- and plate-related quantities. Spatial derivatives are denoted by $(\bullet)_{,i}$ and only right-handed rectangular coordinate systems are used.

2 THE MATHEMATICAL MODEL

The reference configuration is denoted by $V = \Omega \times T \subset \mathbb{R}^3$, where $\Omega \subset \mathbb{R}^2$ is the mid-surface and $T = (-\frac{t}{2}, \frac{t}{2}) \subset \mathbb{R}$ with t the thickness. Γ is the boundary of Ω. Considering a local orthonormal system $\{\boldsymbol{e}_i^r\}$ on the mid-surface with $\boldsymbol{e}_\alpha^r$ tangent and $\boldsymbol{e}_3^r$ normal to it, the reference mid-surface position, normal director and position of a material point are respectively

$$\boldsymbol{\zeta} = \xi_\alpha \boldsymbol{e}_\alpha^r, \quad \boldsymbol{a}^r = \xi_3 \boldsymbol{e}_3^r \quad \text{and} \quad \boldsymbol{\xi} = \boldsymbol{\zeta} + \boldsymbol{a}^r. \tag{1}$$

Let $\boldsymbol{z}$ be the position on the mid-surface at the current configuration, ∇ the gradient operator w.r.t. $\boldsymbol{\zeta}$ and $\mathbf{E}_3^r = \operatorname{skew}(\boldsymbol{e}_3^r)$ the skew-symmetric tensor of its axial vector $\boldsymbol{e}_3^r$. The mid-surface displacement and rotation yield

$$\boldsymbol{u} = \boldsymbol{z} - \boldsymbol{\zeta} \quad \text{and} \quad \boldsymbol{\theta} = -\boldsymbol{e}_3^r \times \nabla u_3 = -\mathbf{E}_3^r \nabla u_3, \tag{2}$$

respectively. They lead to the current mid-surface position, director and position of a material point as

$$\boldsymbol{z} = \boldsymbol{\zeta} + \boldsymbol{u}, \quad \boldsymbol{a} = \mathbf{Q}\boldsymbol{a}^r \quad \text{and} \quad \boldsymbol{x} = \boldsymbol{z} + \boldsymbol{a}, \tag{3}$$

respectively, where $\mathbf{Q} = \mathbf{I} + \boldsymbol{\Theta}$ is the linear rotation tensor with $\mathbf{I}$ the identity matrix and $\boldsymbol{\Theta} = \operatorname{skew}(\boldsymbol{\theta})$.

The relation between the reference and current configurations of a fiber is given by the deformation gradient

$$\mathbf{F} = \boldsymbol{x}_{,i} \otimes \boldsymbol{e}_i^r = (\boldsymbol{z}_{,\alpha} + \boldsymbol{\theta}_{,\alpha} \times \boldsymbol{a}^r) \otimes \boldsymbol{e}_\alpha^r + \boldsymbol{e}_3 \otimes \boldsymbol{e}_3^r = \mathbf{Q} + (\boldsymbol{\eta}_\alpha + \boldsymbol{\kappa}_\alpha \times \boldsymbol{a}^r) \otimes \boldsymbol{e}_\alpha^r, \tag{4}$$

where $\boldsymbol{e}_i = \mathbf{Q}\boldsymbol{e}_i^r$, and the stretch and curvature are respectively defined as

$$\boldsymbol{\eta}_\alpha = \boldsymbol{z}_{,\alpha} - \boldsymbol{e}_\alpha \quad \text{and} \quad \boldsymbol{\kappa}_\alpha = \boldsymbol{\theta}_{,\alpha}. \tag{5}$$

The linear strain and Cauchy stress tensors for an isotropic linear elastic material yield

$$\mathbf{E} = \frac{1}{2}(\mathbf{F} + \mathbf{F}^T - 2\mathbf{I}) \quad \text{and} \quad \mathbf{T} = \lambda(\mathbf{I} : \mathbf{E})\mathbf{I} + 2\mu\mathbf{E} = \boldsymbol{t}_i \otimes \boldsymbol{e}_i^r, \tag{6}$$

respectively, with $\lambda = \frac{E\nu}{(1-2\nu)(1+\nu)}$ and $\mu = \frac{E}{2(1+\nu)}$ (shear modulus) the Lamé constants, E the Young modulus, ν the Poisson ratio and the true stresses $\boldsymbol{t}_i$ acting at the planes with normal $\boldsymbol{e}_i^r$. The plane stress condition is imposed by E_{33} s.t. $T_{33}(E_{33}) = 0$. The internal force and moment per unit length may then be given by the cross-sectional resultants

$$\boldsymbol{n}_\alpha = \int_T \boldsymbol{t}_\alpha \, \mathrm{d}\xi_3 \quad \text{and} \quad \boldsymbol{m}_\alpha = \int_T \boldsymbol{a}^r \times \boldsymbol{t}_\alpha \, \mathrm{d}\xi_3, \tag{7}$$

respectively. By the external body force per unit volume $\boldsymbol{f}^b$ and surface traction per unit area $\boldsymbol{f}^s$, the external force and moment per unit area respectively yield

$$\bar{\boldsymbol{n}} = \int_T \boldsymbol{f}^b \,\mathrm{d}\xi_3 + \boldsymbol{f}^s \quad \text{and} \quad \bar{\boldsymbol{m}} = \int_T \boldsymbol{a}^r \times \boldsymbol{f}^b \,\mathrm{d}\xi_3 + \boldsymbol{a}^r \times \boldsymbol{f}^s. \tag{8}$$

Defining the generalized vectors

$$\boldsymbol{\sigma}_\alpha \coloneqq \begin{bmatrix} \boldsymbol{n}_\alpha & \boldsymbol{m}_\alpha \end{bmatrix}^T, \quad \boldsymbol{\varepsilon}_\alpha \coloneqq \begin{bmatrix} \boldsymbol{\eta}_\alpha & \boldsymbol{\kappa}_\alpha \end{bmatrix}^T, \quad \boldsymbol{q} \coloneqq \begin{bmatrix} \bar{\boldsymbol{n}} & \bar{\boldsymbol{m}} \end{bmatrix}^T \quad \text{and} \quad \boldsymbol{g} \coloneqq \begin{bmatrix} \boldsymbol{u} & \boldsymbol{\theta} \end{bmatrix}^T, \tag{9}$$

the internal virtual work yields

$$\begin{aligned} a(\boldsymbol{u}, \boldsymbol{v}) &= \int_\Omega \boldsymbol{\sigma}_\alpha(\boldsymbol{u}) \cdot \boldsymbol{\varepsilon}_\alpha(\boldsymbol{v}) \,\mathrm{d}\zeta \\ &= -\int_\Omega (\nabla \cdot \mathbf{N}(\boldsymbol{u}) \cdot \boldsymbol{v} - \nabla \cdot \nabla \cdot \mathbf{M}(u_3) v_3) \,\mathrm{d}\zeta \\ &\quad + \int_\Gamma (\mathbf{N}(\boldsymbol{u}) : \boldsymbol{v} \otimes \boldsymbol{\nu} + \mathbf{M}(u_3) : \nabla v_3 \otimes \boldsymbol{\nu} - \nabla \cdot \mathbf{M}(u_3) \cdot \boldsymbol{\nu} v_3) \,\mathrm{d}\tau, \end{aligned} \tag{10}$$

where the divergence theorem, $\nabla\cdot$ the divergence operator w.r.t. $\boldsymbol{\zeta}$, $\boldsymbol{v} \coloneqq \delta\boldsymbol{u}$ a virtual displacement, $\mathbf{N} = \boldsymbol{n}_\alpha \otimes \boldsymbol{e}_\alpha^r$, $\mathbf{M} = \mathbf{E}_3^r \boldsymbol{m}_\alpha \otimes \boldsymbol{e}_\alpha^r$ and $\boldsymbol{\nu}$ the unit outer normal were used. The external virtual work results

$$(\boldsymbol{q}, \boldsymbol{g}(\boldsymbol{v})) = \int_\Omega \boldsymbol{q} \cdot \boldsymbol{g}(\boldsymbol{v}) \,\mathrm{d}\zeta. \tag{11}$$

For instance, let Γ be clamped, $\mathcal{H}^s(\Omega)$ be a Sobolev space and

$$\boldsymbol{\mathcal{V}}_0 \coloneqq [\mathcal{H}_0^1(\Omega)]^2 \times \mathcal{H}_0^2(\Omega) = \{\boldsymbol{v} \in [\mathcal{H}^1(\Omega)]^2 \times \mathcal{H}^2(\Omega) : \boldsymbol{v}|_\Gamma = \boldsymbol{0}, v_{3,\nu}|_\Gamma = 0\}. \tag{12}$$

The theorem of virtual work or weak form of the continuous problem yields

$$\begin{cases} \boldsymbol{u} \in \boldsymbol{\mathcal{V}}_0 \\ a(\boldsymbol{u}, \boldsymbol{v}) = (\boldsymbol{q}, \boldsymbol{g}(\boldsymbol{v})), \quad \forall \boldsymbol{v} \in \boldsymbol{\mathcal{V}}_0 \end{cases}. \tag{13}$$

3 THE DISCRETE MODEL

Ω is now the computational domain decomposed into non-overlapping flat triangles $\mathfrak{E}$ embedded in $\mathbb{R}^3$ from a domain decomposition $\mathcal{T}^h$ s.t. $\Omega = \cup_{\mathfrak{E}\in\mathcal{T}^h} \mathfrak{E}$. Henceforth, superscripts $\mathfrak{E}$, $\mathfrak{e}$ and $\mathfrak{v}$ are for element-, edge- and vertex-wise defined quantities, respectively, and superscript h are for approximated quantities.

The canonical basis of $\mathbb{R}^3$ is denoted by $\{\boldsymbol{e}_i^r\}$ and the local-to-global transformation matrix defined as $\mathbf{R} = \boldsymbol{e}_i^{r,g} \otimes \boldsymbol{e}_i^r$, where superscript g is for a quantity referred to the global system. We also consider a local orthonormal system $\{\boldsymbol{\tau}_i^g, \boldsymbol{\nu}_i^g, -\boldsymbol{e}_3^{r,g}\}$ at an element edge $\mathfrak{e}_i$, where the tangent $\boldsymbol{\tau}_i^g$ is oriented counterclockwise and $\boldsymbol{\nu}_i^g$ is the outer normal. The corresponding local-to-global transformation matrix will be $\mathbf{R}_i^{\mathfrak{e}} = \boldsymbol{\tau}_i^g \otimes \boldsymbol{e}_1^r + \boldsymbol{\nu}_i^g \otimes \boldsymbol{e}_2^r - \boldsymbol{e}_3^{r,g} \otimes \boldsymbol{e}_3^r$. These transformation

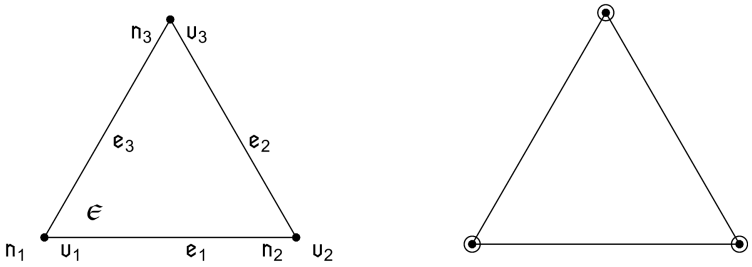

Figure 1: Element components (left) and d.o.f.s of displacement "•" and deflection gradient "◯" (right)

matrices allow to respectively express the displacement, rotation and deflection gradient referred to the correspondent local systems as

$$\boldsymbol{v} = \mathbf{R}^T \boldsymbol{v}^g, \quad \boldsymbol{\theta}(\mathfrak{e}_i) = (\mathbf{R}_i^{\mathfrak{e}})^T \boldsymbol{\theta}^g \quad \text{and} \quad \nabla v_3(\mathfrak{e}_i) = \theta_2(\mathfrak{e}_i)\boldsymbol{\tau}_i - \theta_1(\mathfrak{e}_i)\boldsymbol{\nu}_i. \tag{14}$$

Consider the polynomial approximation orders

$$k_\alpha = 1, \quad k_3 = 2, \quad r = 3, \quad s = k_3 - 1, \quad l = k_\alpha - 2 \quad \text{and} \quad b = k_3 - 4, \tag{15}$$

where we have k_α for the membrane displacement, r for the deflection and s for its normal derivative at the edges. l is for the membrane displacement Laplacian and b for the deflection bi-Laplacian. With $a < 0$ and the convention $\mathbb{P}_a(\mathfrak{E}) = \{0\}$ we have that v_α is harmonic and v_3 is bi-harmonic inside $\mathfrak{E}$.

Let $\boldsymbol{\mathcal{V}}^{\mathfrak{E}} \coloneqq [\mathcal{H}^1(\mathfrak{E})]^2 \times \mathcal{H}^2(\mathfrak{E})$. The local ansatz space is

$$\boldsymbol{\mathcal{V}}^{h,\mathfrak{E}} \coloneqq \{\boldsymbol{v} \in \boldsymbol{\mathcal{V}}^{\mathfrak{E}} : v_\alpha|_{\mathfrak{e}} \in \mathbb{P}_1(\mathfrak{e}), v_3|_{\mathfrak{e}} \in \mathbb{P}_3(\mathfrak{e}), v_{3,\nu}|_{\mathfrak{e}} \in \mathbb{P}_1(\mathfrak{e}), \Delta v_\alpha = \Delta^2 v_3 = 0, \forall \mathfrak{e} \subset \Gamma^{\mathfrak{E}}\} \tag{16}$$

with Δ the Laplace operator w.r.t. $\boldsymbol{\zeta}$. The d.o.f. operator $\chi_i^j : \mathcal{V}_i^{h,\mathfrak{E}} \to \mathbb{R}$ and the canonical basis functions $\varphi_i^j \in \mathcal{V}_i^{h,\mathfrak{E}}$ are defined such that the Kronecker delta property holds accordingly. In this context, superscripts τ and ν denote tangent- and normal-derivative-related quantities, respectively. Let us define the local d.o.f. set as (see Fig. 1)

$$\mathcal{D}^{\mathfrak{E}} \coloneqq \{\boldsymbol{\chi}^i(\boldsymbol{v}), \chi_3^{i,\tau}(v_3), \chi_3^{i,\nu}(v_3)\}, \tag{17}$$

where

$$\boldsymbol{\chi}^i(\boldsymbol{v}) = \boldsymbol{v}(\mathfrak{n}_i), \quad \chi_3^{i,\tau}(v_3) = v_{3,\tau}(\mathfrak{n}_i) \quad \text{and} \quad \chi_3^{i,\nu}(v_3) = v_{3,\nu}(\mathfrak{n}_i). \tag{18}$$

The interpolations are of Lagrange-, Hermite-, and Lagrange-type for the membrane displacements, deflection and its normal derivative, respectively.

The dimension of (16) is

$$\dim(\boldsymbol{\mathcal{V}}^{h,\mathfrak{E}}) \equiv N^{\text{d.o.f.}} = N^{\mathfrak{v}}(2k_\alpha + r + s - 1) = 15, \tag{19}$$

where $N^{(\bullet)}$ means "number of $(\bullet)$". As observed in [6], future investigations on the account of local drilling rotation d.o.f.s need to be performed to avoid the stiffness matrix singularity of coplanar elements.

Let $\boldsymbol{\mathcal{P}}^{\mathfrak{E}} \coloneqq [\mathbb{P}_1(\mathfrak{E})]^2 \times \mathbb{P}_2(\mathfrak{E}) \subset \boldsymbol{\mathcal{V}}^{h,\mathfrak{E}}$ and the ansatz function be decomposed as

$$\boldsymbol{v} = \Pi^{\mathfrak{E}}\boldsymbol{v} + (\mathrm{I} - \Pi^{\mathfrak{E}})\boldsymbol{v}, \quad \forall \boldsymbol{v} \in \boldsymbol{\mathcal{V}}^{h,\mathfrak{E}}, \tag{20}$$

where I is the identity map and $\Pi^{\mathfrak{E}} \equiv \Pi : \boldsymbol{\mathcal{V}}^{h,\mathfrak{E}} \to \boldsymbol{\mathcal{P}}^{\mathfrak{E}}$ a local projector operator. As shown in [7], the latter may be defined s.t., $\forall \boldsymbol{v} \in \boldsymbol{\mathcal{V}}^{h,\mathfrak{E}}$ and $\forall \boldsymbol{p} \in \boldsymbol{\mathcal{P}}^{\mathfrak{E}}$,

$$\begin{cases} \tilde{a}^{\mathfrak{E}}(\boldsymbol{p}, \Pi\boldsymbol{v} - \boldsymbol{v}) = 0 \\ \int_{\mathfrak{E}} (\nabla \Pi_3 v_3 - \nabla v_3)\,\mathrm{d}\zeta = \mathbf{0} \\ \int_{\Gamma^{\mathfrak{E}}} (\Pi\boldsymbol{v} - \boldsymbol{v})\,\mathrm{d}\tau = \mathbf{0} \end{cases} \tag{21}$$

with $\tilde{a}^{\mathfrak{E}}(\boldsymbol{v}, \boldsymbol{v}) \coloneqq \int_{\mathfrak{E}} \boldsymbol{\varepsilon}_\alpha(\boldsymbol{v}) \cdot \boldsymbol{\varepsilon}_\alpha(\boldsymbol{v})\,\mathrm{d}\zeta$. Let the projection be expressed by

$$\Pi\boldsymbol{v} = \boldsymbol{\Pi}\mathfrak{m} = \begin{bmatrix} \pi_{11} & \pi_{12} & \pi_{13} & 0 & 0 & 0 \\ \pi_{21} & \pi_{22} & \pi_{23} & 0 & 0 & 0 \\ \pi_{31} & \pi_{32} & \pi_{33} & \pi_{34} & \pi_{35} & \pi_{36} \end{bmatrix} \begin{bmatrix} 1 & \xi_1 & \xi_2 & \xi_1^2 & \xi_1\xi_2 & \xi_2^2 \end{bmatrix}^T. \tag{22}$$

A test function may be $\boldsymbol{p} = \mathbf{S}\mathfrak{m}$ with $\mathbf{S}$ as $\boldsymbol{\Pi}$ but with arbitrary coefficients. The 1st condition of (21) yields

$$\begin{aligned} \int_{\mathfrak{E}} \boldsymbol{\varepsilon}_\alpha(\boldsymbol{p}) \cdot \boldsymbol{\varepsilon}_\alpha(\Pi\boldsymbol{v})\,\mathrm{d}\zeta &= \int_{\mathfrak{E}} \boldsymbol{\varepsilon}_\alpha(\boldsymbol{p}) \cdot \boldsymbol{\varepsilon}_\alpha(\boldsymbol{v})\,\mathrm{d}\zeta \\ &= \int_{\Gamma^{\mathfrak{E}}} (\tilde{\mathbf{N}}(\boldsymbol{p}) : \boldsymbol{v} \otimes \boldsymbol{\nu} + \tilde{\mathbf{M}}(p_3) : \nabla v_3 \otimes \boldsymbol{\nu} - \nabla \cdot \tilde{\mathbf{M}}(p_3) \cdot \boldsymbol{\nu} v_3)\,\mathrm{d}\tau, \end{aligned} \tag{23}$$

where $\tilde{\mathbf{N}} = \boldsymbol{\eta}_\alpha \otimes \boldsymbol{e}_\alpha^r$ and $\tilde{\mathbf{M}} = \mathbf{E}_3^r \boldsymbol{\kappa}_\alpha \otimes \boldsymbol{e}_\alpha^r$. The left-hand side of (23) may be exactly computed over the boundary by the divergence theorem, since it only has polynomials. The right-hand side may be directly computed in terms of all local d.o.f.s since the ansatz functions are known over the edges. As only $\boldsymbol{\varepsilon}_\alpha(\boldsymbol{p})$ and $\boldsymbol{\varepsilon}_\alpha(\Pi\boldsymbol{v})$ are included in (23), let $N^k \coloneqq \dim(\mathbb{P}_k(\mathfrak{E}))$,

$$\boldsymbol{\pi}_i^a \coloneqq \begin{bmatrix} \pi_{i\,N_i^{\ker}+1} & \dots & \pi_{i\,N^{k_i}} \end{bmatrix}^T \quad \text{and} \quad \boldsymbol{s}_i^a \coloneqq \begin{bmatrix} s_{i\,N_i^{\ker}+1} & \dots & s_{i\,N^{k_i}} \end{bmatrix}^T \tag{24}$$

with $N_\alpha^{\ker} \coloneqq \dim(\ker(a_\alpha^{\mathfrak{E}})) = \dim(\mathbb{P}_0(\mathfrak{E})) = 1$ and $N_3^{\ker} \coloneqq \dim(\ker(a_3^{\mathfrak{E}})) = \dim(\mathbb{P}_1(\mathfrak{E})) = 3$. The consistent part of $\boldsymbol{\Pi}$ follows from, with no summation convention,

$$\mathbf{G}_i \coloneqq \frac{\partial^2 \tilde{a}^{\mathfrak{E}}(\boldsymbol{p}, \Pi\boldsymbol{v})}{\partial \boldsymbol{s}_i^a \partial \boldsymbol{\pi}_i^a}, \quad \boldsymbol{b}_i \coloneqq \frac{\partial \tilde{a}^{\mathfrak{E}}(\boldsymbol{p}, \boldsymbol{v})}{\partial \boldsymbol{s}_i^a}, \quad \mathbf{G}_i \boldsymbol{\pi}_i^a = \boldsymbol{b}_i \quad \text{and} \quad \boldsymbol{\pi}_i^a = \mathbf{G}_i^{-1} \boldsymbol{b}_i. \tag{25}$$

The remainder part of $\boldsymbol{\Pi}$ may then be obtained from the remaining conditions of the equality of deflection gradients and subsequent equality of displacements

$$\int_{\mathfrak{E}} \nabla \Pi_3 v_3 \, \mathrm{d}\zeta = \int_{\mathfrak{E}} \nabla v_3 \, \mathrm{d}\zeta = \int_{\Gamma^{\mathfrak{E}}} v_3 \boldsymbol{\nu} \, \mathrm{d}\tau \quad \text{and} \quad \int_{\Gamma^{\mathfrak{E}}} \Pi \boldsymbol{v} \, \mathrm{d}\tau = \int_{\Gamma^{\mathfrak{E}}} \boldsymbol{v} \, \mathrm{d}\tau, \tag{26}$$

respectively. Both are computable over the edges as is the 1st condition.

By (19), $\dim(\boldsymbol{\mathcal{P}}^{\mathfrak{E}}) < \dim(\boldsymbol{\mathcal{V}}^{h,\mathfrak{E}})$ due to the plate ansatz. Let $\boldsymbol{\mathcal{V}}^{h,\mathfrak{E}}$ be expressed by

$$\boldsymbol{\mathcal{V}}^{h,\mathfrak{E}} = \boldsymbol{\mathcal{P}}^{\mathfrak{E}} \oplus \boldsymbol{\mathcal{P}}^{\mathfrak{E},\perp}, \tag{27}$$

the direct sum, where $\boldsymbol{\mathcal{P}}^{\mathfrak{E},\perp} \subset \boldsymbol{\mathcal{V}}^{h,\mathfrak{E}}$ is the orthogonal complement of $\boldsymbol{\mathcal{P}}^{\mathfrak{E}}$. Let $\boldsymbol{v} \in \boldsymbol{\mathcal{V}}^{h,\mathfrak{E}}$. As mentioned in (20), $\boldsymbol{v} = \Pi \boldsymbol{v} + (\mathrm{I} - \Pi)\boldsymbol{v} = \Pi \boldsymbol{v} + \boldsymbol{v}^{\perp}$ with $\Pi \boldsymbol{v} \in \boldsymbol{\mathcal{P}}^{\mathfrak{E}}$ and $\boldsymbol{v}^{\perp} \in \boldsymbol{\mathcal{P}}^{\mathfrak{E},\perp}$. A stabilization potential energy containing $\boldsymbol{v}^{\perp}$ needs to be computed, being a natural choice to consider the d.o.f. remainders. We follow the procedure as in [7] and consider the continuous counterpart of the classical stabilization (see e.g. [8]):

$$U_{\text{int}}^{\mathfrak{E},\perp} \coloneqq \frac{1}{2} \frac{E t^3}{12(1-\nu^2)} \sum_{i=1}^{N^{\mathfrak{e}}} \int_{\mathfrak{e}_i} (|\mathfrak{E}|^{-1} v_3^{\perp}(\mathfrak{e}_i) v_3^{\perp}(\mathfrak{e}_i) + \nabla v_3^{\perp}(\mathfrak{e}_i) \cdot \nabla v_3^{\perp}(\mathfrak{e}_i)) \, \mathrm{d}\tau. \tag{28}$$

The internal potential energy can finally be written as

$$U_{\text{int}}^{h,\mathfrak{E}} = U_{\text{int}}^{\mathfrak{E}}(\Pi \boldsymbol{v}^h) + U_{\text{int}}^{\mathfrak{E},\perp}(v_3^h), \tag{29}$$

where $U_{\text{int}}^{\mathfrak{E}}(\Pi \boldsymbol{v}^h) = \frac{1}{2} a^{\mathfrak{E}}(\Pi \boldsymbol{v}^h, \Pi \boldsymbol{v}^h)$ must be, in contrast to $U_{\text{int}}^{\mathfrak{E},\perp}$, exactly computed.

In the following the need of (28) will be eliminated by the SFVEM for the present application. One of its procedure main steps is to define the curvature $\mathcal{L}^2$-projector to a polynomial space of a certain convenient order l_3. For $(k_\alpha, k_3) = (1, 2)$, the ansatz (16) contains the space of constant curvatures: we have Hermite cubic deflections over the edges thus quadratic normal rotations and linear correspondent curvatures. Additionally, the linear tangent rotations lead to their constant curvatures. For $N^{\mathfrak{e}} = 3$, it follows that $\dim(\mathbb{P}_2(\mathfrak{E})) < \dim(\mathcal{V}_3^{h,\mathfrak{E}}) < \dim(\mathbb{P}_3(\mathfrak{E}))$. Thus, at first sight one may say that l_3 must be at least 1 in this case to yield a linear curvature approximation, representing cubic deflections. We empirically show that this is indeed the case. In other words, we choose

$$l_3 = l_3(k_3, N^{\mathfrak{e}}) = k_3 - 1 + N^{\mathfrak{e}} - 3. \tag{30}$$

Let $\boldsymbol{v} \in \boldsymbol{\mathcal{V}}^{h,\mathfrak{E}}$. We define the $\mathcal{L}^2$-projector of the curvature field as $\Pi_1^{0,\alpha} \boldsymbol{\kappa}_\alpha(\bullet) : \mathcal{H}^2(\mathfrak{E}) \to \boldsymbol{\mathcal{P}}_1^{0,\mathfrak{E}} \coloneqq [\mathbb{P}_1(\mathfrak{E})]^2 \times \{0\}$ s.t.

$$(\boldsymbol{\lambda}_\alpha, \Pi_1^{0,\alpha} \boldsymbol{\kappa}_\alpha(v_3) - \boldsymbol{\kappa}_\alpha(v_3))^{\mathfrak{E}} = 0, \quad \forall \boldsymbol{\lambda}_\alpha \in \boldsymbol{\mathcal{P}}_1^{0,\mathfrak{E}}. \tag{31}$$

Let the projection be expressed by

$$\Pi_1^{0,\alpha} \boldsymbol{\kappa}_\alpha = \boldsymbol{\Pi}_1^{0,\alpha} \mathfrak{m} = \begin{bmatrix} \pi_{11}^{0,\alpha} & \pi_{12}^{0,\alpha} & \pi_{13}^{0,\alpha} \\ \pi_{21}^{0,\alpha} & \pi_{22}^{0,\alpha} & \pi_{23}^{0,\alpha} \\ 0 & 0 & 0 \end{bmatrix} \begin{bmatrix} 1 & \xi_1 & \xi_2 \end{bmatrix}^T. \tag{32}$$

A test function may be $\boldsymbol{\lambda}_\alpha = \mathbf{S}_1^{0,\alpha}\mathfrak{m}$ with $\mathbf{S}_1^{0,\alpha}$ as $\mathbf{\Pi}_1^{0,\alpha}$ but with arbitrary coefficients. The condition (31) yields

$$\begin{aligned}\int_{\mathfrak{E}} \boldsymbol{\lambda}_\alpha \cdot \Pi_1^{0,\alpha}\boldsymbol{\kappa}_\alpha(v_3)\,\mathrm{d}\zeta &= \int_{\mathfrak{E}} \boldsymbol{\lambda}_\alpha \cdot \boldsymbol{\kappa}_\alpha(v_3)\,\mathrm{d}\zeta \\ &= \int_{\mathfrak{E}} \nabla\cdot\nabla\cdot\mathbf{\Lambda} v_3\,\mathrm{d}\zeta + \int_{\Gamma^{\mathfrak{E}}} (\mathbf{\Lambda} : \nabla v_3 \otimes \boldsymbol{\nu} - \nabla\cdot\mathbf{\Lambda}\cdot\boldsymbol{\nu} v_3)\,\mathrm{d}\tau \\ &= \int_{\Gamma^{\mathfrak{E}}} (\mathbf{\Lambda} : \nabla v_3 \otimes \boldsymbol{\nu} - \nabla\cdot\mathbf{\Lambda}\cdot\boldsymbol{\nu} v_3)\,\mathrm{d}\tau,\end{aligned} \tag{33}$$

where $\mathbf{\Lambda} = \mathbf{E}_3^r\boldsymbol{\lambda}_\alpha \otimes \boldsymbol{e}_\alpha^r$. Fortunately, for $l_3 = 1$, $\boldsymbol{\lambda}_\alpha \in \boldsymbol{\mathcal{P}}_1^{0,\mathfrak{E}}$ and $\int_{\mathfrak{E}} \nabla\cdot\nabla\cdot\mathbf{\Lambda} v_3\,\mathrm{d}\zeta = 0$, simplifying the procedure since the deflection is unknown inside $\mathfrak{E}$. As usual, we set

$$\boldsymbol{\pi}_\beta^{0,\alpha} \coloneqq \begin{bmatrix}\pi_{\beta\,1}^{0,\alpha} & \pi_{\beta\,2}^{0,\alpha} & \pi_{\beta\,3}^{0,\alpha}\end{bmatrix}^T \quad \text{and} \quad \boldsymbol{s}_\beta^{0,\alpha} \coloneqq \begin{bmatrix}s_{\beta\,1}^{0,\alpha} & s_{\beta\,2}^{0,\alpha} & s_{\beta\,3}^{0,\alpha}\end{bmatrix}^T, \tag{34}$$

to get the curvature $\mathcal{L}^2$-projector from, with no summation convention,

$$\begin{aligned}&\mathbf{G}_\beta^{0,\alpha} \coloneqq \frac{\partial^2(\boldsymbol{\lambda}_\alpha, \Pi_1^{0,\alpha}\boldsymbol{\kappa}_\alpha)^{\mathfrak{E}}}{\partial \boldsymbol{s}_\beta^{0,\alpha}\partial\boldsymbol{\pi}_\beta^{0,\alpha}}, \quad \boldsymbol{b}_\beta^{0,\alpha} \coloneqq \frac{\partial(\boldsymbol{\lambda}_\alpha, \boldsymbol{\kappa}_\alpha)^{\mathfrak{E}}}{\partial \boldsymbol{s}_\beta^{0,\alpha}}, \quad \mathbf{G}_\beta^{0,\alpha}\boldsymbol{\pi}_\beta^{0,\alpha} = \boldsymbol{b}_\beta^{0,\alpha} \quad \text{and} \\ &\boldsymbol{\pi}_\beta^{0,\alpha} = (\mathbf{G}_\beta^{0,\alpha})^{-1}\boldsymbol{b}_\beta^{0,\alpha}.\end{aligned} \tag{35}$$

Four systems of linear equations corresponding to the two components of each curvature vector then emerge.

Let $\boldsymbol{v} \in \boldsymbol{\mathcal{V}}^{h,\mathfrak{E}}$. Finally, the self-stabilized internal potential energy takes the form:

$$U_{\text{int}}^{h,\mathfrak{E}} = \frac{1}{2}\int_{\mathfrak{E}} (\boldsymbol{n}_\alpha(\Pi\boldsymbol{v})\cdot\boldsymbol{\eta}_\alpha(\Pi\boldsymbol{v}) + \boldsymbol{m}_\alpha(\Pi_1^{0,\alpha}\boldsymbol{\kappa}_\alpha)\cdot\Pi_1^{0,\alpha}\boldsymbol{\kappa}_\alpha)\,\mathrm{d}\zeta. \tag{36}$$

For the external potential energy we specialize (11) with $\bar{\boldsymbol{m}} = \mathbf{0}$ to consider (see e.g. [8, 9])

$$U_{\text{ext}}^{h,\mathfrak{E}} = -\langle \bar{\boldsymbol{n}}^{h,g}, \boldsymbol{v}^{h,g}\rangle^{\mathfrak{E}} = -|\mathfrak{E}|\bar{\boldsymbol{n}}^{h,g}.(N^{\mathfrak{v}})^{-1}\sum_{i=1}^{N^{\mathfrak{v}}} \boldsymbol{v}^{h,g}(\mathfrak{v}_i). \tag{37}$$

The residual and stiffness matrix referred to the global system yield

$$\boldsymbol{r}^{h,\mathfrak{E}} = \frac{\partial U^{h,\mathfrak{E}}}{\partial\boldsymbol{\mathfrak{d}}} \quad \text{and} \quad \mathbf{K}^{h,\mathfrak{E}} = \frac{\partial\boldsymbol{r}^{h,\mathfrak{E}}}{\partial\boldsymbol{\mathfrak{d}}}, \tag{38}$$

where $U^{h,\mathfrak{E}} = U_{\text{int}}^{h,\mathfrak{E}} + U_{\text{ext}}^{h,\mathfrak{E}}$ is the total potential energy and $\boldsymbol{\mathfrak{d}} \coloneqq \left[\boldsymbol{g}^{h,g}(\mathfrak{n}_i)\right]^T$ the d.o.f. vector. Respective assemblages result

$$\boldsymbol{r}^h = \sum_{\mathfrak{E}\in\mathcal{T}^h} \boldsymbol{r}^{h,\mathfrak{E}} \quad \text{and} \quad \mathbf{K}^h = \sum_{\mathfrak{E}\in\mathcal{T}^h} \mathbf{K}^{h,\mathfrak{E}}, \tag{39}$$

and the minimum of potential energy discrete form is

$$\begin{cases}\boldsymbol{u}^h \in \boldsymbol{\mathcal{V}}^h \\ \boldsymbol{r}^h = \mathbf{0}\end{cases}. \tag{40}$$

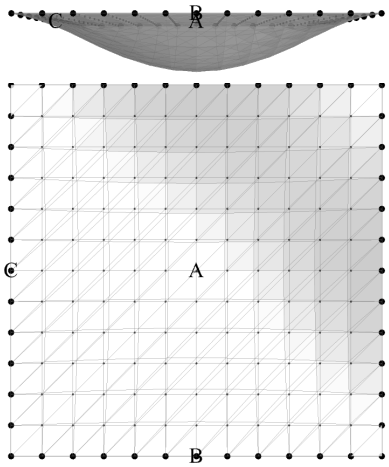

Figure 2: Simply supported plate: $\mathfrak{E}_2$ reference and current configurations

4 RESULTS

The elements and numerical results were respectively implemented and computed with the Wolfram Mathematica software system and the AceSystem, see e.g. [10]. Three elements will be denoted by $\mathfrak{E}_i$: $\mathfrak{E}_1$ is based on the conventional VEM, i.e. on (29); $\mathfrak{E}_2$ is based on the SFVEM, i.e. on (36); $\mathfrak{E}_3$ is based on the consistent conventional VEM, i.e. only on the first term of (29) right-hand side. All values are referred to the global system, the domain coordinates are given by $\{x_i\}$, N_i denotes the total number of d.o.f.s for a particular element $\mathfrak{E}_i$, and the superscripts h and g are eliminated. The current configurations are in true scale, and the Euclidean norm and the relative error ε are considered.

For all examples consider $-\frac{1}{2} \leq x_1, x_2 \leq \frac{1}{2}$, $t = 10^{-4}$, body load $f_3^b = -8 \times 10^3$, $E = 2 \times 10^{11}$ and $\nu = 0.3$.

4.1 Simply supported plate

Consider $x_3 = 0$ and a simply supported Γ (see Fig. 2). The analytical Kirchhoff solution is used (see e.g. [11]).

The displacement and rotation colormaps for a particular mesh refinement are depicted in Figs. 3, 4 and 5. Good agreement between $\mathfrak{E}_1$ and $\mathfrak{E}_2$ is seen and the absence of stabilization is visualized by the discontinuity of the $\mathfrak{E}_3$ rotations.

The solutions curves are displayed in Fig. 6. Displacement results of $\mathfrak{E}_2$ are interestingly better and the rotation ones are almost identical compared to results of $\mathfrak{E}_1$, presenting also asymptotic convergence. This shows in this example that the curvature order (30) of the self-stabilized plate is sufficient. Accordingly with the presented colormaps, the numerical instability is evident for the rotations of $\mathfrak{E}_3$. The same does not occur for the $\mathfrak{E}_3$ displacement, showing that the projection space may be sufficient to obtain satisfactory and numerically stable deflection results for a triangular element.

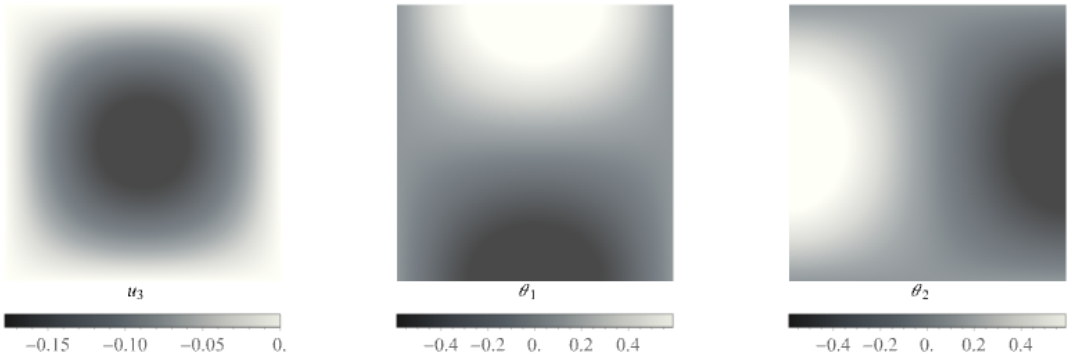

Figure 3: Simply supported plate: displacement and rotation colormaps for $\mathfrak{E}_1$

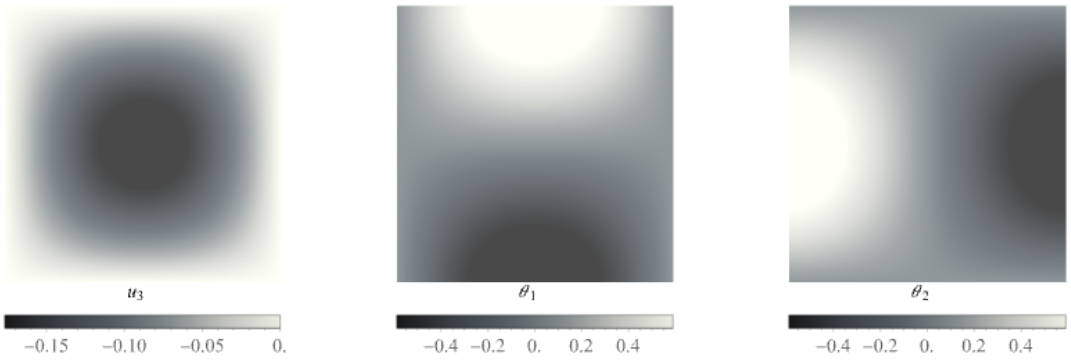

Figure 4: Simply supported plate: displacement and rotation colormaps for $\mathfrak{E}_2$

4.2 Partially clamped hyperbolic paraboloid shell

Consider $x_3 = x_1^2 - x_2^2$, $t = 10^{-2}, 10^{-3}, 10^{-4}$, and Γ partially clamped on $x_1 = -\frac{1}{2}$ and free on the remaining boundary (see Fig. 7). Reference solutions are the extrapolation values found in Tables 17 and 18 of [12].

Fig. 8 shows the results from $\mathfrak{E}_2$ getting better as the structure gets thinner, compared to $\mathfrak{E}_1$. In contrast, for the thicker cases, the $\mathfrak{E}_2$ convergence is slower and with higher relative errors. Nevertheless, the errors obtained by $\mathfrak{E}_2$ on a fine mesh result similar for all the thickness cases. The SFVEM model seems more sensitive to the thickness in shell problems, which does not occur in the previous plane problem. This scenario will be further investigated in future works.

5 CONCLUSIONS

This work presents a self-stabilized triangular virtual element for linear Kirchhoff–Love shells. The importance of the stabilization is visualized by a simple example and a self-stabilized

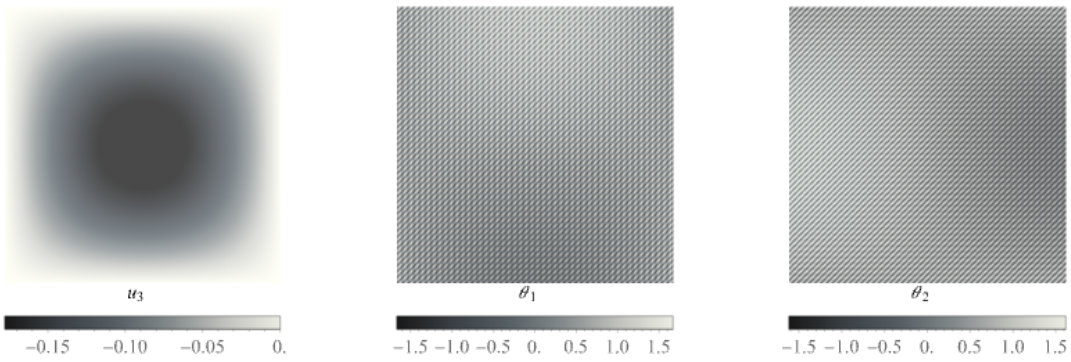

Figure 5: Simply supported plate: displacement and rotation colormaps for $\mathfrak{E}_3$

triangular shell element was successfully tested. Satisfactory accuracy is reached in the numerical results when compared to its conventional version which has a stabilization potential energy. Nonetheless, further investigations on its behavior regarding the thickness influence in shell applications should be performed. Possible future works include element geometry, approximation order and nonlinear behavior generalizations, and the minimum curvature polynomial order (30) validation also for nonconforming virtual Kirchhoff plate elements.

REFERENCES

[1] Da Veiga, L.B., Brezzi, F., Cangiani, A., Manzini, G., Marini, L.D., Russo, A. Basic principles of Virtual Element Methods. *Mathematical Models and Methods in Applied Sciences.* (2013) **23**(01):199–214.

[2] Berrone, S., Borio, A., Marcon, F. Lowest order stabilization free Virtual Element Method for the 2D Poisson equation. *arXiv preprint arXiv:2103.16896.* (2021).

[3] Chen, A., Sukumar, N. Stabilization-free Virtual Element Method for plane elasticity. *Computers & Mathematics with Applications.* (2023) **138**:88–105.

[4] Chen, A., Sukumar, N. Stabilization-free Serendipity Virtual Element Method for plane elasticity. *Computer Methods in Applied Mechanics and Engineering.* (2023) **404**:115784.

[5] Xu, B.B., Peng, F., Wriggers, P. Stabilization-free Virtual Element Method for finite strain applications. *Computer Methods in Applied Mechanics and Engineering.* (2023) **417**:116555.

[6] Wu, T.P., Pimenta, P.M., Wriggers, P. On triangular virtual elements for Kirchhoff–Love shells. *Archive of Applied Mechanics.* (2024) 1–34.

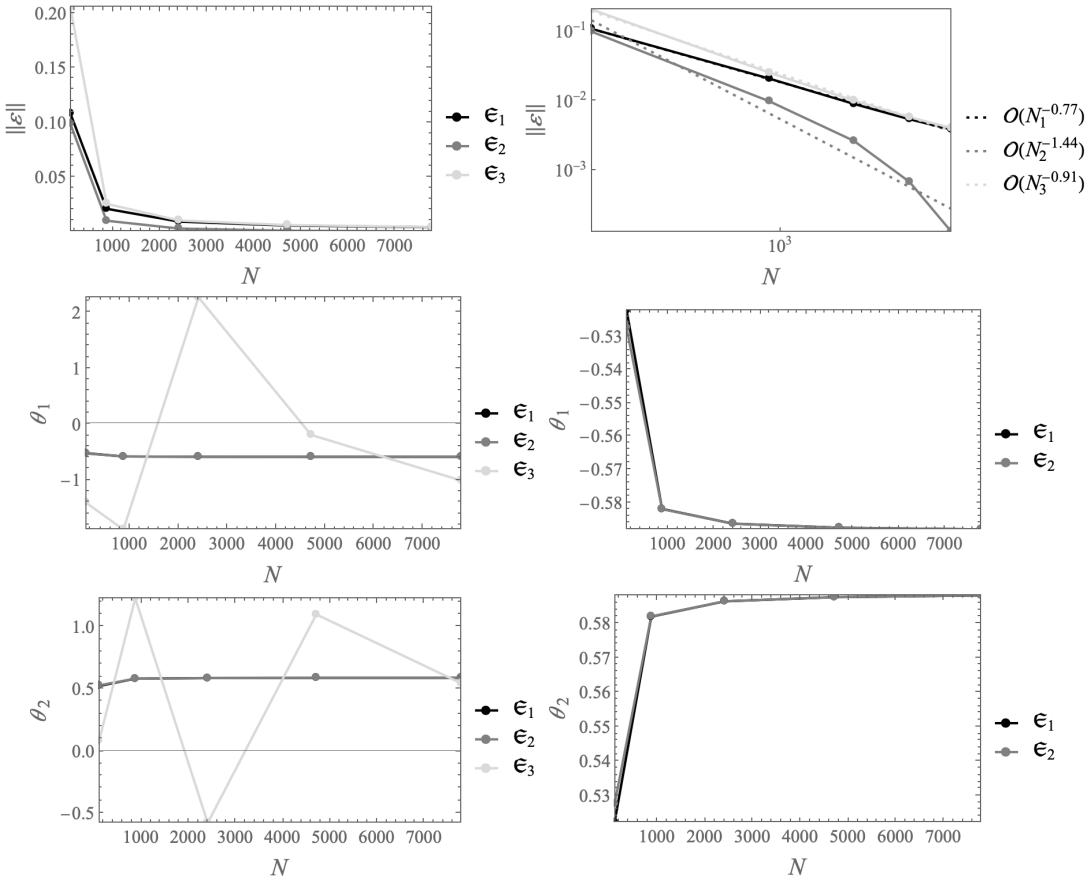

Figure 6: Simply supported plate: convergence curves of displacement at point "A" (top), and rotations at points "B" (center) and "C" (bottom)

[7] Wriggers, P., Hudobivnik, B., Allix, O. On two simple virtual Kirchhoff-Love plate elements for isotropic and anisotropic materials. *Computational Mechanics.* (2022) **69**(2):615–637.

[8] Brezzi, F., Marini, L.D. Virtual Element Methods for plate bending problems. *Computer Methods in Applied Mechanics and Engineering.* (2013) **253**:455–462.

[9] Mengolini, M., Benedetto, M.F., Aragón, A.M. An engineering perspective to the Virtual Element Method and its interplay with the standard Finite Element Method. *Computer Methods in Applied Mechanics and Engineering.* (2019) **350**:995–1023.

[10] Korelc, J., Wriggers, P. Automation of Finite Element Methods. *Springer.* (2016).

[11] Timoshenko, S., Woinowsky-Krieger, S. Theory of plates and shells. *McGraw Hill.* (1959).

[12] Krysl, P., Chen, J.S. Benchmarking computational shell models. *Archives of Computational Methods in Engineering.* (2023) **30**(1):301–315.

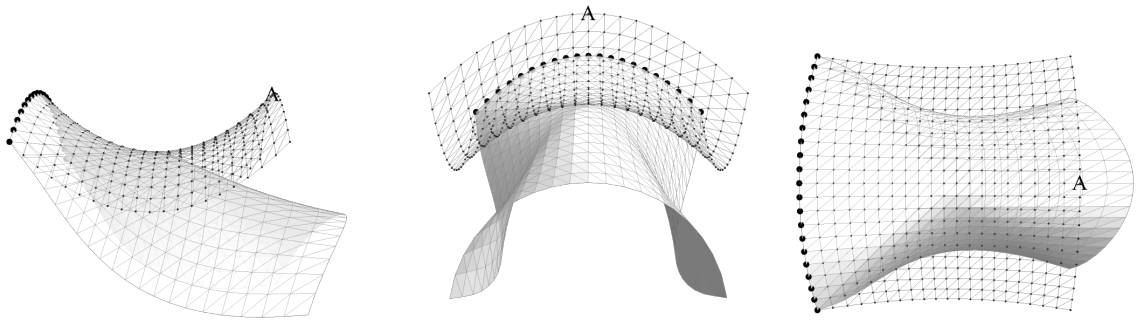

Figure 7: Partially clamped hyperbolic paraboloid shell: $\mathfrak{E}_2$ reference and current configurations

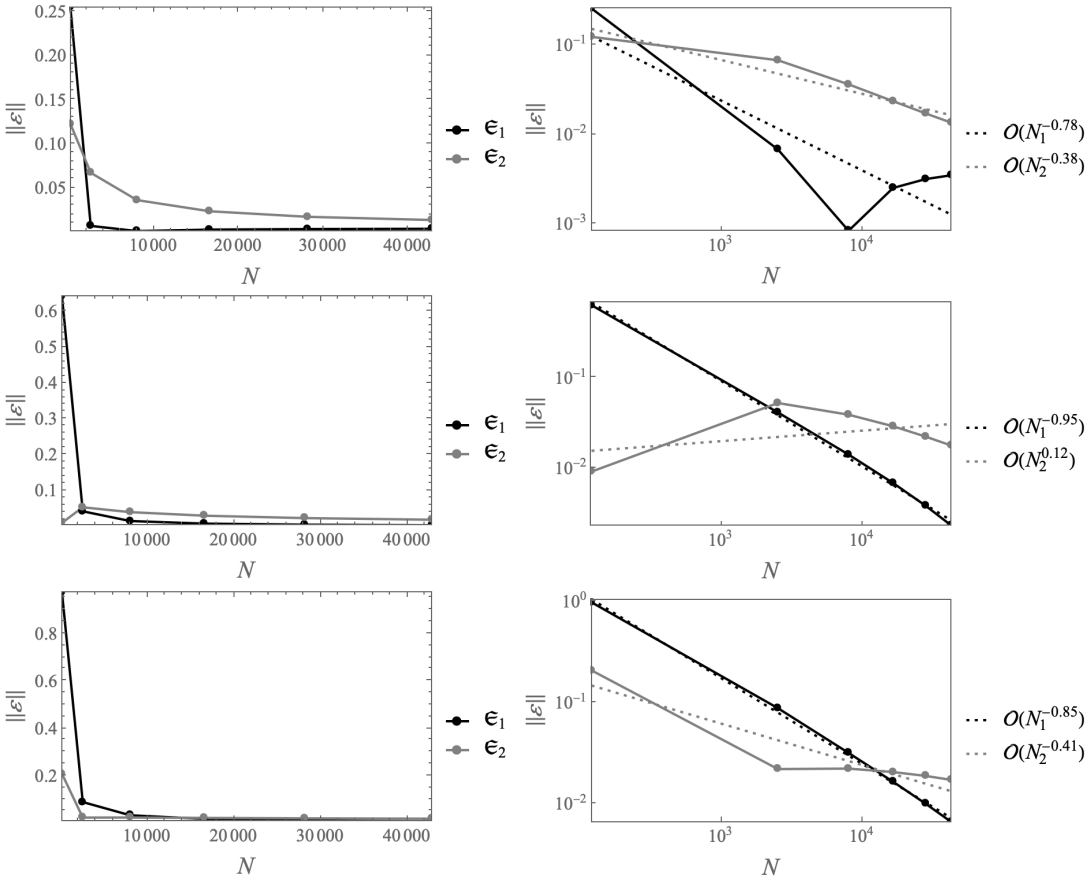

Figure 8: Partially clamped hyperbolic paraboloid shell: convergence curves for $t = 10^{-2}$ (top), $t = 10^{-3}$ (center) and $t = 10^{-4}$ (bottom)